Available online at www.sciencedirect.com
SCIENCE DIRECT®
ELSEVIER
Icarus 168 (2004) 324–335
ICARUS
www.elsevier.com/locate/icarus

# A re-analysis of the 1971 Beta Scorpii occultation by Jupiter: study of temperature fluctuations and detection of wave activity

Elisabeth Raynaud, Katia Matcheva,[1] Pierre Drossart,* Françoise Roques, and Bruno Sicardy

*LESIA, CNRS–UMR 8109, Observatoire de Paris, 5 place Jules Janssen, 92195 Meudon CEDEX, France*

Received 19 March 2003; revised 26 August 2003

**Abstract**

Data from the 13 May 1971 $\beta$ Scorpii occultation by the southern polar region of Jupiter (Vapillon et al., 1973, Astron. Astrophys. 29, 135–149) are re-analyzed with current methods. We correct the previous results for an inacurrate background estimation and calculate new temperature profiles, that are now consistent with the results of other observers of this occultation, as well as with the current knowledge of the jovian atmosphere. The characteristics of the profiles of temperature gradient and the spectral behavior of the temperature fluctuations are found to be similar to the results of previous investigations of planetary atmospheres and in agreement with the presence of atmospheric propagating gravity waves in the jovian atmosphere. We use a wavelet analysis of the temperature profiles to identify the dominant modes of wave activity and compare the reconstructed temperature fluctuations to model-generated gravity waves.


*Keywords:* Jupiter; Occultations; Atmospheres, structure; Dynamics

## 1. Introduction

On 13 May 1971, $\beta$ Scorpii was occulted by the southern hemisphere of Jupiter. The two brightest components of this multi-star system are $\beta$ Sco $A(V = 2.76)$ and $\beta$ Sco $C(V = 2.94)$, separated by 13 arcsec in position angle $P = 64°$ (the position angle express the relative position of two stars: it is the angle between the line joining them and the celestial north direction). The occultations by the two components could be observed separately. The star $\beta$ Sco $A$ is an unresolved spectroscopic binary of spectral type $B0.5V$ and period 6.8 days, and has a fainter companion $\beta$ Sco $B(V \sim 10)$, at 0.5 arcsec in position angle $P = 24°$. The star $\beta$ Sco $C$ is of spectral type $B2V$. The 1971 occultation by Io revealed that it is a double star (Bartholdi and Owen, 1972) and has a fainter companion at 0.1 arcsec.

The $\beta$ Scorpii occultation provided an unprecedented opportunity to study the jovian upper atmosphere. This was the first time in nearly twenty years (since the occultation of $\sigma$ Arietis, with $V = 5.5$, observed by Baum and Code in 1953) that such an important event took place. Therefore it was observed from various locations and analyzed by three groups: the 'Meudon group' led by M. Combes and J. Lecacheux (Combes et al., 1971), the 'Texas group' led by W.B. Hubbard (Hubbard et al., 1972) and the 'Cornell group' led by J. Veverka (Veverka et al., 1974). Occultations of the unresolved $\beta$ Sco $A$ system, and $\beta$ Sco $C$ allowed the different groups to constrain the radius of Jupiter (Hubbard and Van Flandern, 1972; Lecacheux et al., 1973), and to retrieve density and temperature profiles of the jovian upper atmosphere (Hubbard et al., 1972; Vapillon et al., 1973; Veverka et al., 1974). However, although the probed chords on the planet were rather close, the different teams retrieved very different results concerning the derived temperature profiles. The Meudon group obtained temperature profiles with a very large negative gradient, close to $-1.5\,\mathrm{K\,km^{-1}}$, and temperatures of 350 K at a pressure level of 1 mbar (Vapillon et al., 1973). The Texas group has published only refractivity profiles, but the temperatures related to these profiles show a smaller negative gradient, of about $-0.6\,\mathrm{K\,km^{-1}}$ (Hubbard et al., 1972). The Cornell group retrieved a quasi-isothermal profile, with temperature values around 200 K (Veverka et al., 1974), depending on the ratio of helium to hydrogen that was uncertain at that time.

In this paper, we re-analyze the Meudon data using the knowledge acquired since 1971, as well as new techniques

* Corresponding author.
*E-mail address:* pierre.drossart@obspm.fr (P. Drossart).
[1] Present address: Department of Astronomy, Space Sciences Building, Cornell University, Ithaca, NY 14853, USA.

0019-1035/$ – see front matter 
doi:10.1016/j.icarus.2003.10.021

for occultation data study. Section 2 is devoted to data re-analysis with modern tools. In Section 3, after discussing the importance of an accurate estimation of the background flux, we fit isothermal lightcurves to the data in order to derive the scale height $H$, and perform an inversion to obtain temperature profiles.

The subject of wave activity in Jupiter's upper and middle atmosphere has been a topic of discussion in a number of previous investigations. Analyzing the temperature profiles resulting from the inversion of the $\beta$ Sco lightcurves of the Cornell group, French and Gierasch (1974) pointed out the presence of small amplitude variations. They concluded that the observed quasi-periodic temperature fluctuations were consistent with the propagation of internal gravity waves. They determined a typical vertical wavelength of 13 km and an amplitude of 5 K for the waves present in the egress temperature profile of the jovian stratosphere, at a density level of $10^{13}\,\mathrm{cm}^{-3}$. The 1999 occultation of HIP 9369 by the northern polar region of Jupiter also showed evidence for propagating waves in the same pressure regime (Raynaud et al., 2003). The occultation was observed from four different locations. Correlation studies of the resulting lightcurves and a wavelet analysis of the retrieved temperature profiles were used to identify a single wave mode propagating along the planetary meridian with vertical and horizontal wavelengths of respectively 3 and 70 km. Signatures of gravity waves have been also detected at lower pressure levels. The temperature profile derived from the deceleration rate of the Galileo probe during its entry stage in the thermosphere of Jupiter shows a variability with a typical scale from 90 to 150 km (Young et al., 1997). The presence of regularly spaced layers of enhanced electron density observed during the radio occultations of the Voyager and the Galileo spacecraft has also been attributed to the propagation of atmospheric gravity waves and their interaction with the ionospheric plasma (Matcheva et al., 2001). The electron density profiles suggest a typical vertical scale of 75 km for the present waves.

In the current study we use a wavelet analysis to determine the parameters of the dominant wave modes present in the upper stratosphere of Jupiter, as revealed by the $\beta$ Scorpii stellar occultation observed by the Meudon group (Section 4). In that respect our results are complementary to the wave analysis of French and Gierasch (1974). The use of the forward wavelet transform allows us to study in great detail the amplitude, the phase and the vertical wavelength behavior of the present waves. We then utilize the inverse wavelet transform as a tool to reconstruct temperature fluctuations at selected scales and compare the results to the properties of model-generated gravity waves (Section 5).

## 2. Re-analysis of the 1971 Meudon data

The Meudon group observed the $\beta$ Sco occultation in the Ca II K line ($\lambda = 0.3934$ μm) from Radcliffe Observatory, situated in South Africa (28°13′43.7″ E, 25°47′16.9″ S). Observational details can be found in Combes et al. (1971). The star path on Jupiter, recalculated from Hipparcos data and the JPL ephemeris calculation site,[2] is shown in Fig. 1. We digitalized the occultation lightcurves from the data charts of 1971. The scanning procedure was checked and yielded curves identical to those published by Vapillon et al. (1973) (see Fig. 2).

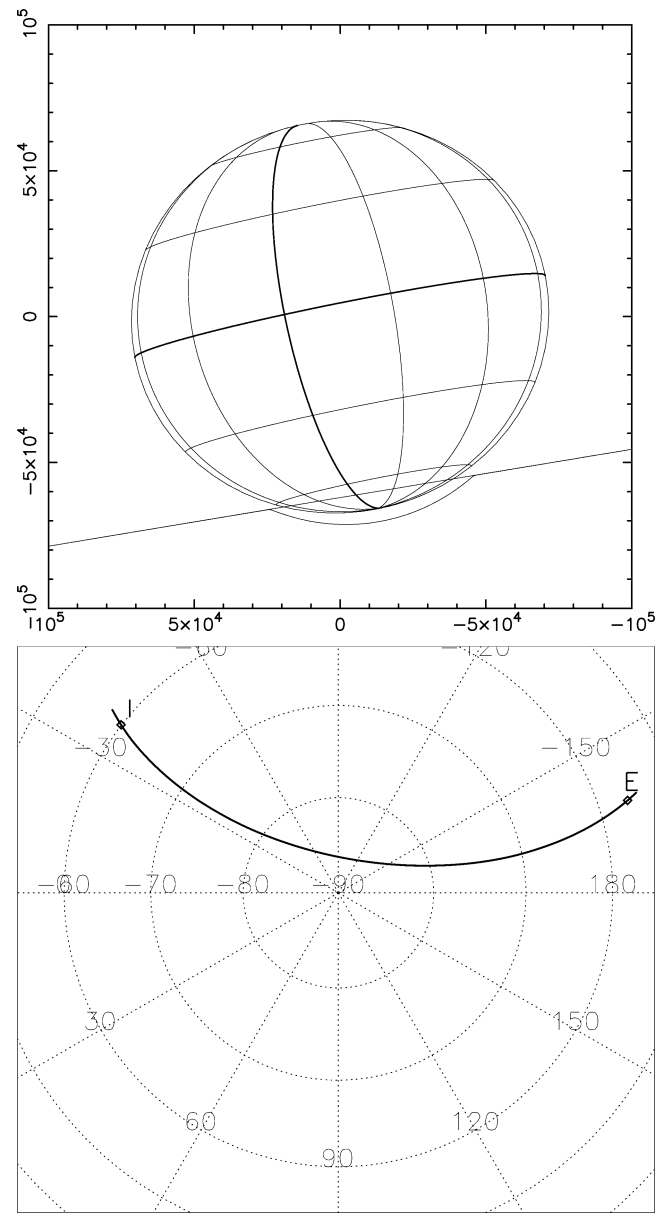


Fig. 1. Star path in reference to the planet. Upper panel: path of $\beta$ Sco $A$, in the sky plane, centered at the center of Jupiter. The position angle of the poles' axis in this frame is 11.32°. Lower panel: stellar path on the planet on a polar view. Half-light points for ingress and egress are plotted on the stellar path, their jovian coordinates are respectively (58.69° S, 322.38° W) and (56.24° S, 197.67° W) with system III longitudes.

[2] http://ssd.jpl.nasa.gov/horizons.html.

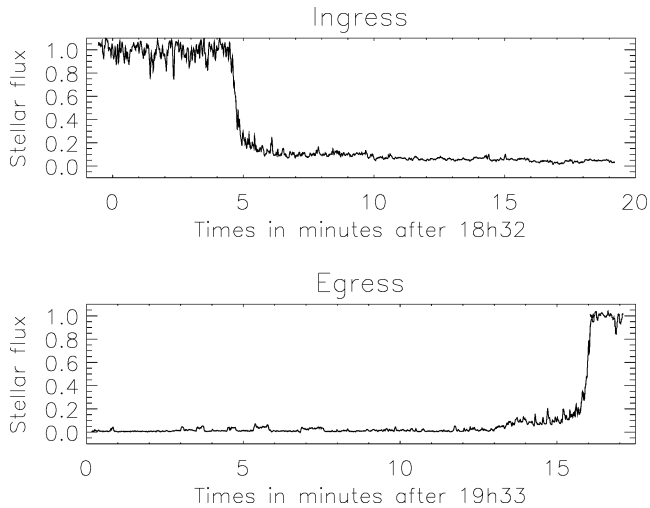


Fig. 2. Ingress (top panel) and egress (bottom panel) normalized lightcurves.

We analyze the data presented in Fig. 2 using the two classical methods for occultation lightcurves, reviewed in Wasserman and Veverka (1973): lightcurve fitting with atmospheric models on the one side, and numerical abelian inversion on the other side. These methods were also used by the Meudon group in 1971 to obtain the published results. However, today's progress in numerical analysis and the improved computing capabilities allow us to obtain more accurate results. For ingress and egress, we first calculate a dimensionless measure of the noise $\epsilon\sqrt{v_\perp/H}$, where $\epsilon$ is the rms variance per second of the normalized unocculted flux, $v_\perp$ the star speed perpendicular to the limb, and $H$ the scale height (French et al., 1978). We obtain noise values of 0.018 for ingress and 0.021 for egress, showing that the noise level is sufficiently low for an accurate inversion (Young et al., 2001). Following Baum and Code (1953), we generate model lightcurves for an isothermal atmosphere in order to obtain the best fit to the data, and thus estimate the scale height $H$ of the atmosphere. Our best fit yields scale heights of $H = 34.9 \pm 1.6$ km for ingress, and $H = 34.6 \pm 0.9$ km for egress (the errors are fitting errors only). These numbers are consistent with the 1971 estimation of $H = 30 \pm 5$ km (Combes et al., 1971). However, they are large compared to the values derived from the 1989 equatorial occultation by Hubbard et al. (1995) (yielding $H = 27.2$ km at ingress and $H = 30$ km at egress), as well as to those obtained by Raynaud et al. (2003) ($24.8 < H < 29.7$ km for eight lightcurves) for the 1999 occultation by the northern polar region.

We invert the lightcurves using the method described in Vapillon et al. (1973). We calculate the pressure equipotentials of the planet with the following equation:

$$U(r,\theta) = -\frac{GM}{r}\left[1 - \sum_{n=2,4,6} J_n \left(\frac{a}{r}\right)^n P_n(\cos\theta)\right] - \frac{1}{2}\omega^2 r^2 \sin^2\theta, \quad (1)$$

where $P_n$ are Legendre polynomials, $\omega$ the rotating angular speed of the planet, $J_n$ the gravitational moments of Jupiter, and $a$ the equatorial radius. The gravitational field is then obtained by $\vec{g} = -\vec{\nabla}U$. The value of the helium abundance ratio well below the homopause is set to the value measured by the Galileo probe (von Zahn et al., 1998). A vertical profile of helium abundance is then generated using a diffusion equation, with the value of the eddy diffusion coefficient fixed to $K = 2 \times 10^6\ \mathrm{cm^2\,s^{-1}}$, (Drossart et al., 2000) and extrapolated at the latitudes of occultation along the pressure equipotentials. From the helium abundance vertical profile, we then obtain the molecular mass and specific refractivity profiles needed for a correct inversion. The inverted temperature profiles obtained for both ingress and egress are displayed in Fig. 3 and agree with those of Vapillon et al. (1973).

These profiles are highly unlikely for several reasons. Firstly, the very large negative temperature gradient exceeds the adiabatic gradient

$$\left(\frac{\partial T}{\partial z}\right)_{ad} = -\Gamma = -g/c_p = -1.81\,\mathrm{K\,km^{-1}}$$

(where $c_p$ is the specific heat at constant pressure) in several points (marked with crosses in Fig. 3). That would suggest that the atmosphere is convectively unstable at these levels, a result which is not supported by observations (Seiff et al., 1996). Secondly, the high temperatures at pressures $P > 100$ µbar (Fig. 3) are not compatible with the $CH_4$ emission in the $\nu_4$ band at 7.8 µm, as observed by Voyager/IRIS (Hanel et al., 1979). Such temperatures extrapolated to the 10 mbar pressure level lead to a methane emission that is 70 (270) times higher for ingress (egress) than the observed value (Orton et al., 1991). Thirdly, the jovian atmosphere is now known to be roughly isothermal below the 10 µbar level, due to radiative equilibrium between $CH_4$ emission and solar flux absorption (Yelle et al., 2001). The profiles from Vapillon et al. (1973), shown in Fig. 3, are thus not credible.

## 3. Estimation of the background flux

It has been shown before (Roques et al., 1994; Raynaud et al., 2003) that the inverted temperature profiles are dependent on the photometric quality of the data: the unocculted stellar flux influences the shape of the profile above the half-light level, and the background level changes the bottom value of the temperature profile. An inaccurate estimation of the background flux during the occultation could be the cause for the inconsistencies in the inversion results we have pointed out. Berezne et al. (1975) explained how this background flux was calculated and claimed a 1% photometric accuracy for the lightcurves of Vapillon et al. (1973). However, their calculation was based on the hypothesis that the contribution of the jovian limb is only proportional to the disk area seen by the photometer and that the inaccuracies

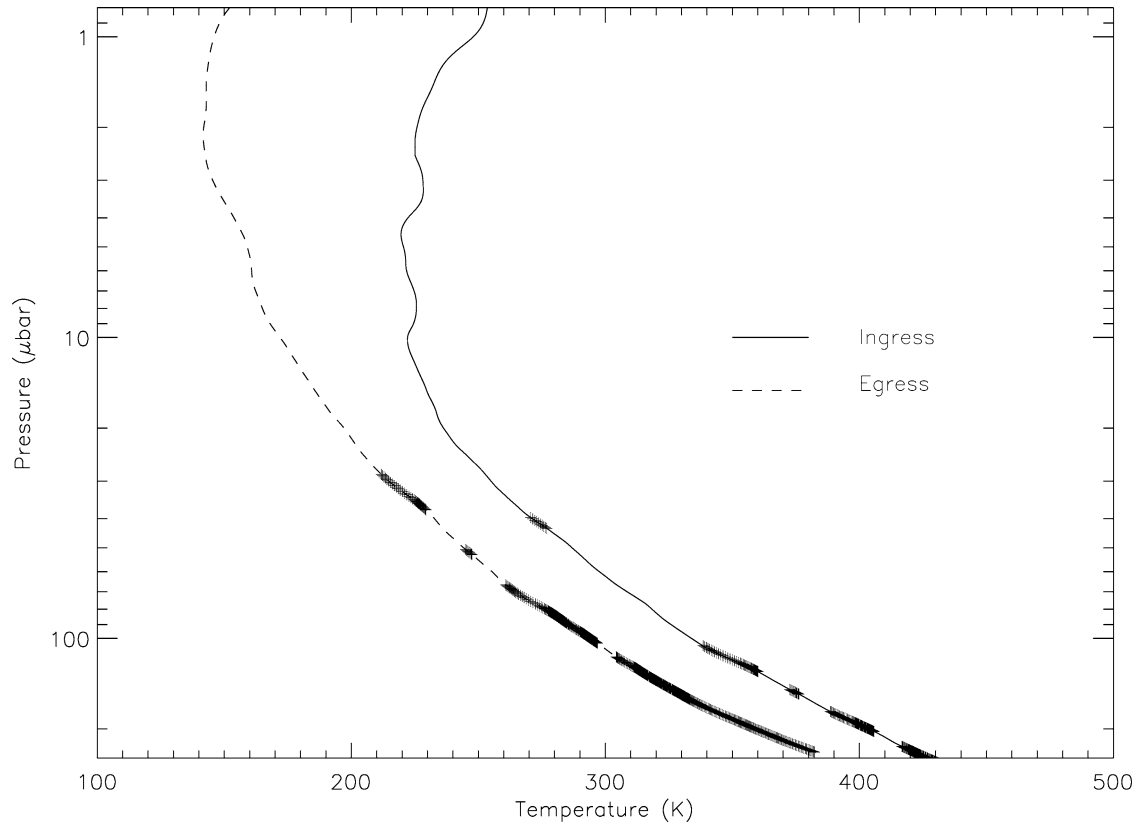


Fig. 3. Temperature profiles obtained by inversion of the lightcurves in Fig. 2, for a background flux equal to 0. Ingress temperature profile is in full line, and egress profile is in dashed line. Crosses on the profiles mark the points where the temperature gradient is super-adiabatic.

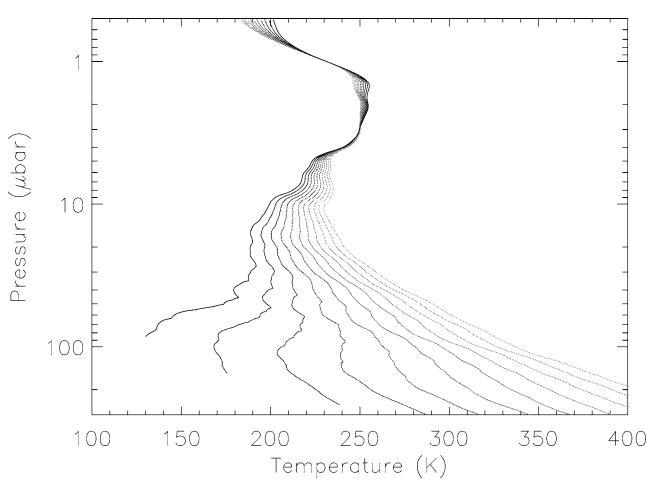


Fig. 4. Inverted temperature profiles, for ingress, for values of background flux going from $\phi_0 = 0$ to $\phi_0 = 0.1$, with a 0.01 step. The darker curves are the ones with smaller $\phi_0$.

of the manual guiding were negligible. To check the relevance of their background estimation, we invert the ingress lightcurve imposing different background levels $\phi_0$, from their estimated value $\phi_0 = 0$ to $\phi_0 = 0.1$. The results are shown in Fig. 4. We can see that a background flux between 0.08 and 0.09 gives a nearly isothermal profile. To determine a more accurate value of $\phi_0$, we perform new isothermal fits to the lightcurves, leaving the background flux as a free parameter. Fitting only the external parts of the lightcurves (i.e., for $t < 18^{\mathrm{h}}42$ UT at ingress, and for $t > 19^{\mathrm{h}}46$ UT at egress), we obtain good fits for $\phi_0 = 0.087 \pm 0.004$, $H = 26.8 \pm 1.7$ km, and $t_{1/2} = 67002.5 \pm 0.4$ s at ingress, and $\phi_0 = 0.068 \pm 0.004$, $H = 24 \pm 0.2$ km, and $t_{1/2} = 71337.1 \pm 0.4$ s at egress. The isothermal fit for ingress is displayed in Fig. 5. The values for the scale heights are now more in the range of previous measurements (see above).

We set the background flux at $\phi_0 = 0.087$ for ingress and $\phi_0 = 0.068$ for egress and invert the resulting lightcurves. We accordingly obtain quasi-isothermal profiles, displayed in Fig. 6. The temperature profiles in Fig. 6 are now more consistent with those of Veverka et al. (1974). They remain convectively stable, and the corresponding bottom temperatures of 190 K for ingress and 150 K for egress are consistent with the observations of methane emission lower in the atmosphere (Orton et al., 1991).

The only need to re-analyze the temperature profiles was to obtain a realistic profile of the atmospheric temperature. This goal has been achieved with a correction of the background stellar flux. In the remaining part of the paper, we shall focus on the analysis of the small scale temperature variations in the retrieved profiles, which are independent of the background flux estimation.

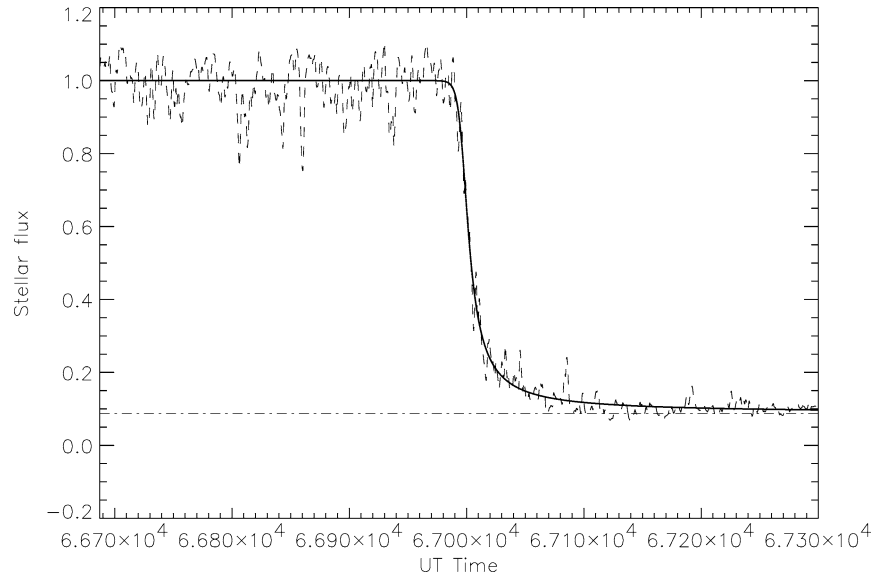


Fig. 5. Isothermal fit (plain solid line) of the observed ingress lightcurve (dotted line) for $\phi_0 = 0.087 \pm 0.004$, $H = 26.8 \pm 1.7$ km, and $t_2 = 67002.5 \pm 0.4$ s. The level of background flux for the best fit is indicated with a dash-dotted line.

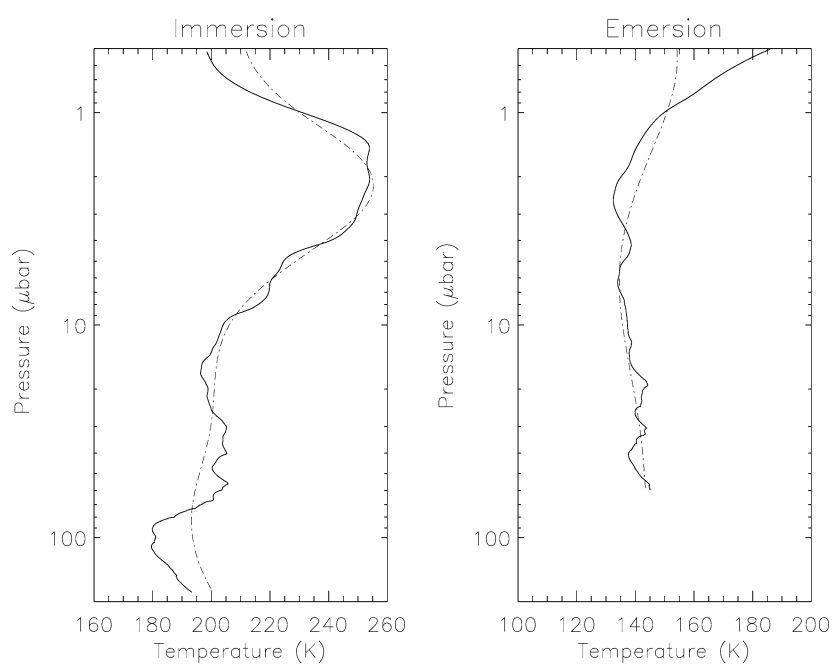


Fig. 6. Temperature profiles obtained with the background levels given in the text, for ingress (left) and egress (right). The mean profiles calculated from the wavelet reconstruction for $\lambda_z > 70$ km (see text) are plotted in dash-dotted line.

## 4. Temperature variations

### 4.1. Temperature gradient

From the temperature profiles in Fig. 6, we calculate the vertical temperature gradient $\partial T/\partial z$, shown in Fig. 7. From now on, our vertical scale will be expressed in kilometers above the half-light level, situated at a pressure of $P \sim 2.8$ µbar. One can see in Fig. 7 that both ingress and egress gradients are very asymmetric. Round shaped structures appear on the negative side, with values close to the adiabatic gradient when the global temperature profile is essentially isothermal, whereas sharp, large peaks can be observed on the positive side. Temperature gradients with similar properties have now been observed in several stellar and radio occultations, by Jupiter (Raynaud et al., 2003) or other planetary bodies such as Neptune (Roques et al., 1994), Venus (Hinson and Jenkins, 1995), or Titan (Sicardy et al., 1999). It is interpreted as a signature of propagating gravity waves, breaking whenever the temperature gradient reaches the adiabatic value (here $-\Gamma = -1.81\,\mathrm{K\,km^{-1}}$), and thus causing the rounded appearance of the temperature gra-

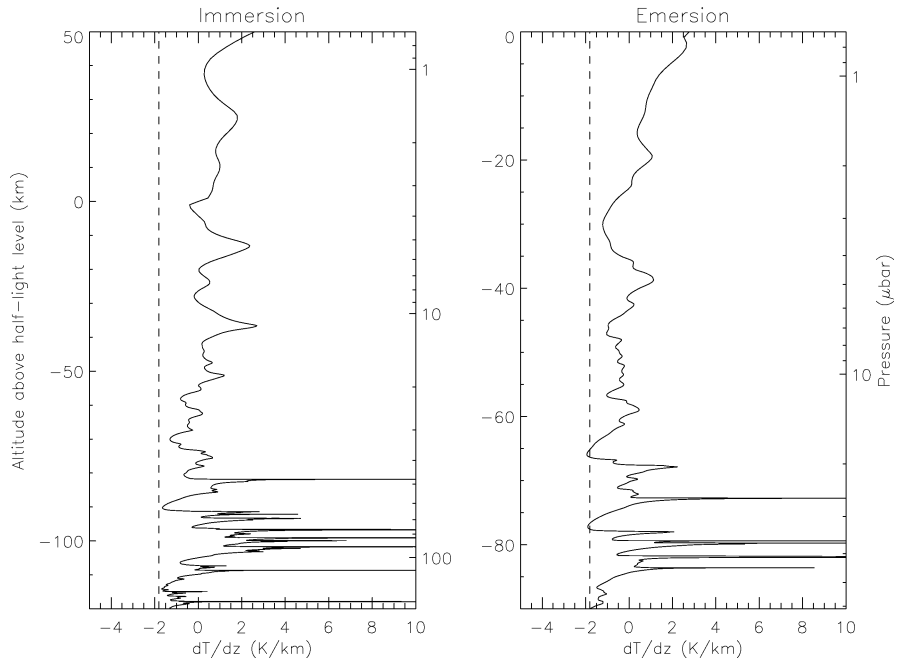


Fig. 7. Temperature gradients for ingress (left) and egress (right). The adiabatic gradient is shown for comparison in dashed line.

dients at negative values. Ray crossing could cause the same kind of asymmetric structures at the lowest altitudes (Sicardy et al., 1999), but would provide no explanation for the visible cut-off precisely at the adiabatic value. The gravity wave interpretation is also consistent with the fact that the vertical scale of the structures is larger in the upper part of the atmosphere ($\sim$ 10–15 km) than at the bottom of the profiles ($\sim$ 1 km). This dependence of the structures' minimum vertical scale with altitude cannot be explained by the flattening of the smoothing star's diameter only: as a matter of fact, the diameter of the unresolved binary $\beta$ Sco $A$ is of the order of 4 km before the occultation (Hubbard et al., 1972) and the vertical resolution at the bottom of the profiles is limited by the Fresnel scale ($\sqrt{\lambda^{\mathrm{obs}} D_{\mathrm{Jup-Earth}}} = 0.5$ km).

### 4.2. Spectral behavior of temperature fluctuations

To extract the small scale fluctuations of temperature from the inverted profile $T(z)$, we need to calculate a mean profile $\langle T \rangle(z)$. We use the continuous wavelet transform (Farge, 1992; Torrence and Compo, 1998) and decompose the temperature profile onto the different scales allowed by the length of the data set. For more detailed information on the continuous wavelet transform and its use for the analysis of occultation data, we refer the reader to Raynaud et al. (2003). The mean temperature profile $\langle T \rangle(z)$ is defined as the reconstruction of the temperature profile using the inverse wavelet transform for scales larger than a given cut-off scale $\lambda_z^{\mathrm{mean}}$. The calculated mean profiles are plotted in Fig. 6 in dash-dotted line ($\lambda_z^{\mathrm{mean}} = 70$ km for a total length of the profile equal to 140 km). The small scale fluctuations, of wavelengths smaller than $\lambda_z^{\mathrm{mean}}$, are then given by $\delta T(z) = T(z) - \langle T \rangle(z)$. We calculate the wavelet power spectrum of the fluctuations, $P_{\delta T(z)}(\lambda_z)$, as a function of the vertical wavelength $\lambda_z$ of the structures in the profiles, and plot it in Fig. 8. A straight line, corresponding to a spectrum $P(m_z) = m_z^{-3}$, where $m_z$ is the vertical wavenumber ($m_z = 2\pi/\lambda_z$), is plotted for comparison. This $-3$ spectral index has been observed on Earth for temperature fluctuations caused by saturated gravity waves, and is referred to, in atmospheric science literature, as the 'universal spectrum' for gravity waves (Smith et al., 1987). For the inverted profiles in this work, the spectra of the fluctuations have also slopes close to $-3$, which is likely to be a signature of the presence of propagating gravity waves.

### 4.3. Determination of dominant wave modes

The observed power spectra of the temperature fluctuations entails the presence of a broad spectrum of atmospheric waves. We now focus our attention on identifying the dominant modes present in the atmosphere and their parameters. For this analysis we use a modified version of the continuous wavelet transform. In the classic wavelet transform, the scaled and translated versions of the mother function are all normalized to have the same energy (Torrence and Compo, 1998). Hence the results from the continuous wavelet transform visualize the energy repartition in the decomposed signal between the different scales $\lambda_z$ for each altitude point. As a result, two monochromatic waves of equal amplitudes but different wavelengths have different wavelet coefficients. In this work we want to compare the amplitudes of the periodic structures and not their energy. In the modified wavelet transform we relax the condition for energy normalization of the individual wavelet functions and require that any two waves with the same amplitude result in equal wavelet coefficient. This modification allows us to study the small scale

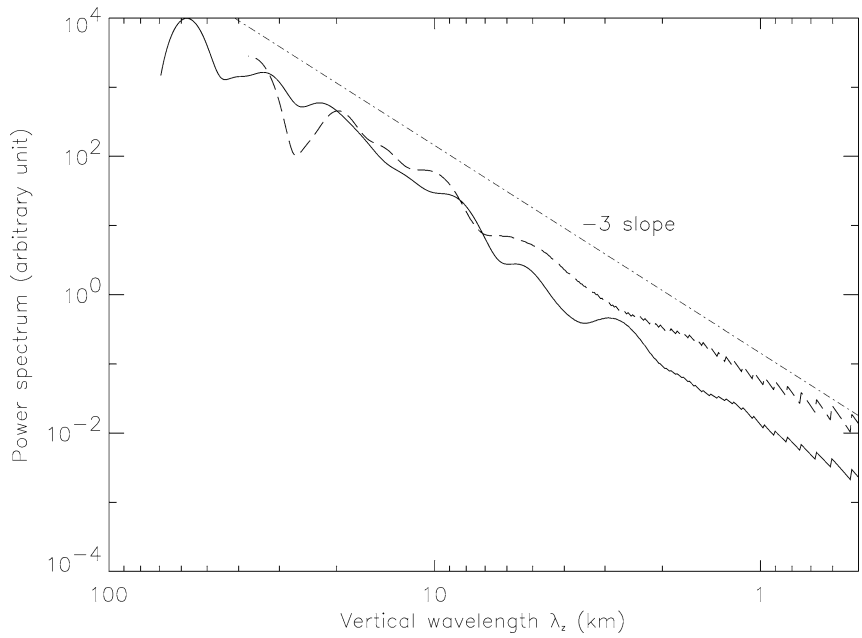


Fig. 8. Power spectra of $\delta T(z)$ (see text) for ingress (full line) and egress (dashed). A line of slope −3 has been plotted for comparison (dash-dotted line).

structures without being overpowered by the large scale fluctuations. The non-normalized wavelet coefficients $A(z, \lambda_z)$ are proportionnal to the amplitude of the fluctuations and vary accordingly with the altitude $z$ and the vertical wavelength $\lambda_z$. The results from the analysis of the ingress and egress temperature profiles are shown as contour maps in Fig. 9. The lowest dark line in Fig. 9 represents a zero amplitude. A cut-off value for the large amplitudes has been imposed for better viewing. We calculate the locations of the local maxima of $A(z, \lambda_z)$ in the $(z, \lambda_z)$ plane and detect 5 maxima for ingress and 4 for egress, which are marked by black stars in Fig. 9. The locations of the maxima in the $(z, \lambda_z)$ plane determine the vertical wavelengths $\lambda_z^{\text{obs}}$ of the wave modes present in the data, and the altitudes where a maximum amplitude is achieved. In order to ensure that the detected wave modes are not due to artefacts of the data inversion and that they are independent of the model parameters, we repeat the analysis using temperature profiles inverted for different values of the background stellar flux (with $0.1 > \phi_0 > 0.06$). Only the modes that are persistently present in all wavelet maps are retained for the next step of our analysis. The vertical wavelengths of these modes are 22.5, 13.9, 9.3, and 2.9 km for the ingress temperature profile, and 10.5, 5.9, and 1.9 km for the egress profile.

## 5. Wave simulations and interpretations

When an atmospheric wave propagates through the atmosphere, the wave amplitude, vertical wavelength and phase are affected by variations in the properties of the background atmosphere. A vertically propagating wave experiences a natural exponential growth of its temperature (velocity) amplitude as a direct consequence of the exponential decrease of the atmospheric density and energy conservation. If the amplitude becomes large enough for the local gradients to exceed the stability criteria (static or dynamic), the wave becomes unstable and overturns. A number of dissipative processes, such as molecular and eddy diffusion, thermal conduction, or radiative damping, can also limit the wave amplitude growth, causing the wave to deposit its energy in the background atmosphere (Lindzen, 1981). But even if the atmosphere is conservative, i.e., there is no dissipation, variations in the background temperature and/or presence of wind shear will cause observable changes in the wave amplitude and vertical wavelength. In our study we exploit this dependence of the wave amplitude, wavelength and phase on local atmospheric properties to positively identify the presence of gravity waves in the retrieved temperature profiles.

We perform a numerical simulation of the wave modes identified in Section 4.3 and compare the simulated wave properties with the observations. We use a hydrostatic WKB wave model in a dissipative rotating atmosphere. Dissipation is due to molecular viscosity, thermal conduction and eddy diffusion. Because no information is available for the wind structure at these altitudes we assume that no wind shear is present. A detailed description of the model can be found in Matcheva and Strobel (1999). The mean temperature profile for the wave simulations is obtained using the wavelet procedure we describe in Section 4.2 with $\lambda_z^{\text{mean}} = 30$ km. The eddy diffusion coefficient is $D_0 = 300\,\text{m}^2\,\text{s}^{-1}$ at the 1 μbar level and decreases as $D \propto \rho^{-0.5}$ (Atreya, 1986), where $\rho$ is the density.

For each of the identified wave modes $\lambda_z^{\text{obs}}$, the numerical simulation is performed with a vertical wavelength that fits the observation at the altitude of the peak in the wavelet map.

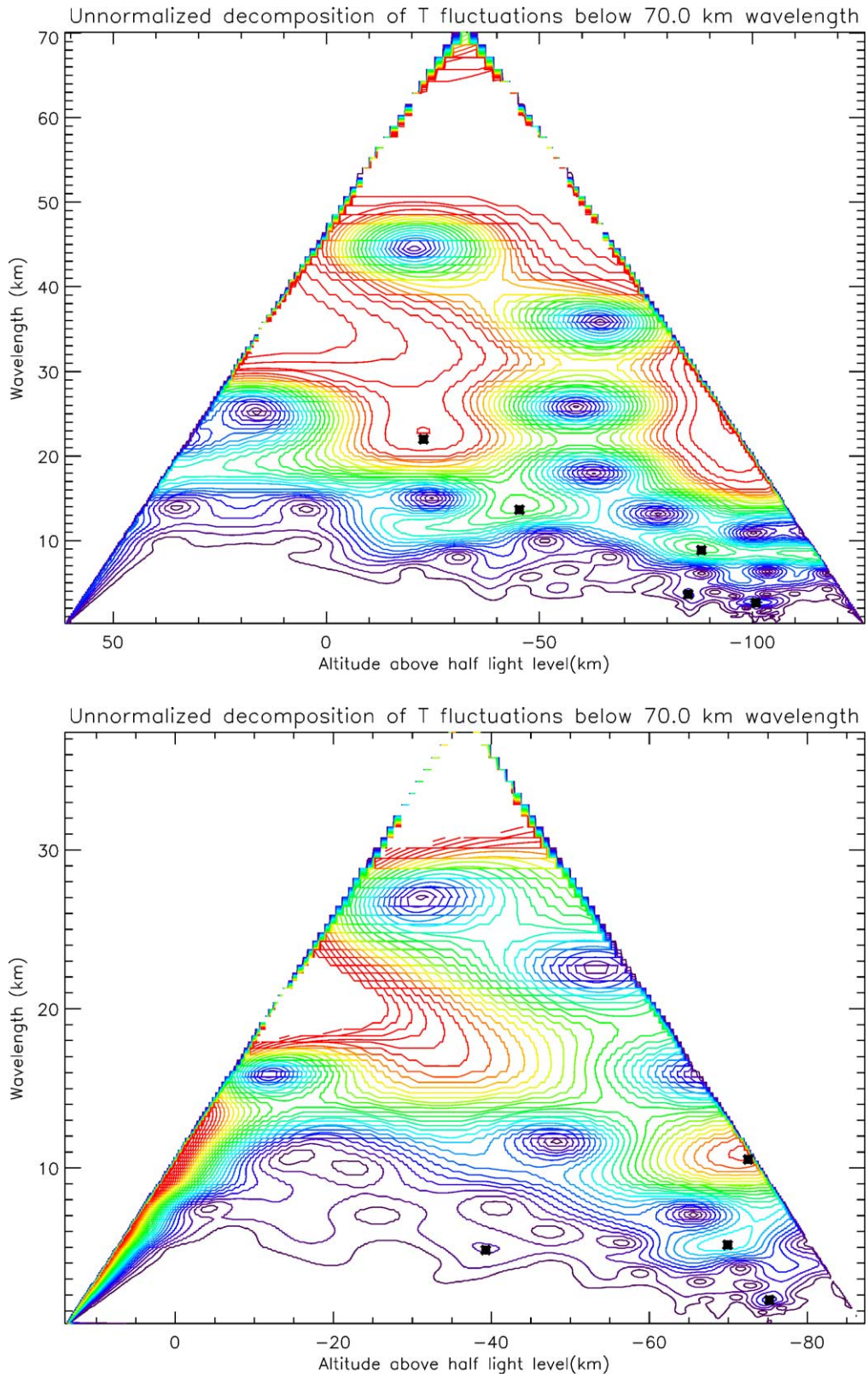


Fig. 9. Amplitude contour maps of the ingress (top panel) and egress (bottom panel) temperature profiles in Fig. 6. The warm colors represent high amplitudes. The local extrema are marked with stars, and their vertical wavelengths $\lambda_z^{\mathrm{obs}}$ are given in the text. The points subject to the edge effects due to the wavelet transform have been excluded from both maps.

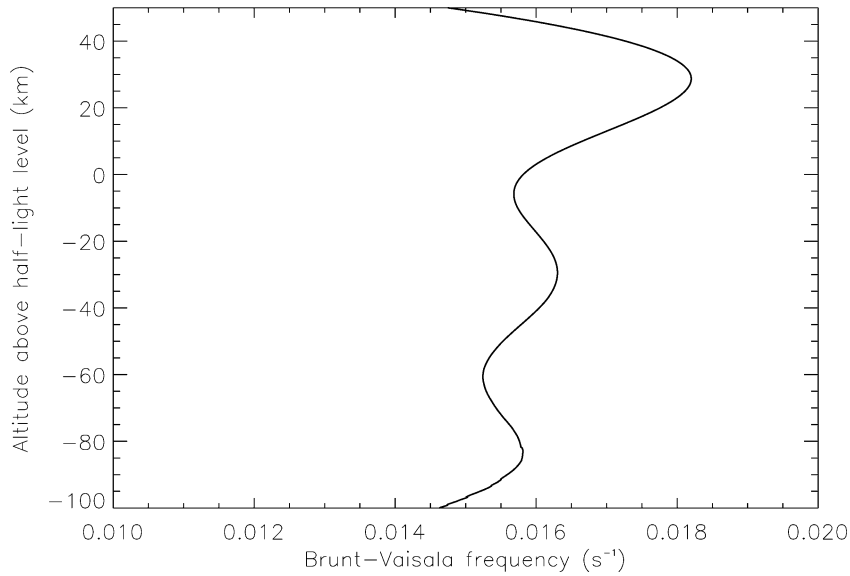


Fig. 10. Brunt–Vaisala frequency for immersion.

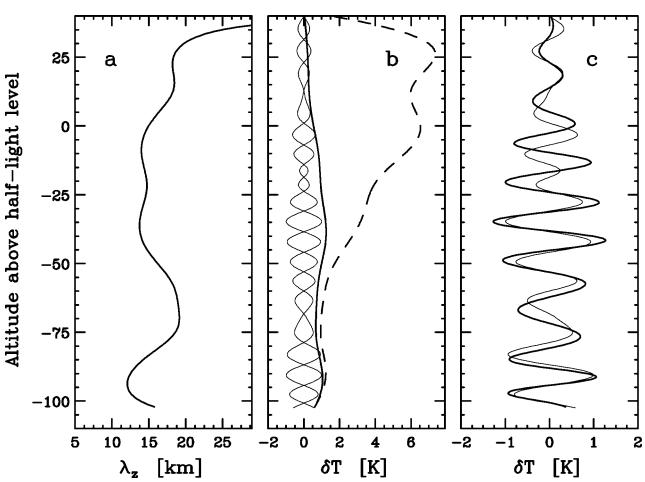


Fig. 11. Analysis of the 13.9 km structure. (a) Vertical wavelength profile for a simulated gravity wave. (b) Comparison between the temperature amplitude of the simulated wave (thick solid line) and the amplitude of the reconstructed temperature fluctuations (thin solid line) for 12 km $< \lambda_z <$ 17 km. The amplitude of the reconstructed wave is represented by the envelope of the actual fluctuations and their mirror image. The dashed line corresponds to the amplitude of the simulated wave when no dissipation is present. (c) Comparison between the phase of the simulated wave (thick solid line) and the reconstructed temperature fluctuations (thin solid line). Here again, both phases have been represented symmetrically for better viewing.

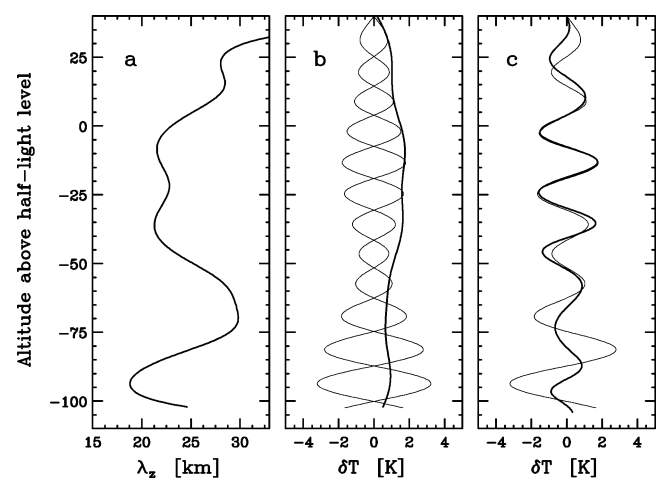


Fig. 12. Same as Fig. 11 but for the 22 km structure.

From the simulation we determine the range $(\lambda_{\min}, \lambda_{\max})$ in which the vertical wavelength changes as a result of background temperature variations. We use the inverse wavelet transform to reconstruct the temperature fluctuations present in the observed temperature profile, using only wavelengths $\lambda_z$ within the expected range $(\lambda_{\min} < \lambda_z < \lambda_{\max})$. The reconstructed temperature fluctuations are then compared with the wave simulations. For completeness, we present a plot of the buoyancy frequency in the region of interest in Fig. 10.

We present one figure with three panels (Figs. 11–14) for each peak in the data wavelet map followed by a discussion in the text. The left panels show the simulated vertical wavelength behavior of the wave as it propagates through the non-isothermal atmosphere. The middle panels compare the reconstructed temperature fluctuations with the simulated wave temperature amplitude, and the right panels show how well the phase of the simulated wave fits the observations.

Ideally one should be able to follow the wave-like structure over several scale heights with at least two scale heights below the altitude of wave damping. The region over which the wavelet analysis returns useful information regarding the present wave modes becomes progressively smaller for larger scales, as a result of the increasing importance of edge effects. Therefore large scale structures are difficult to interpret uniquely as a result of propagating waves.

We start our discussion with the best wave candidate. This is the 13.9 km ingress structure that peaks at approximately −45 km below the mid-occultation level. The peak shows a significant power and is well situated in the middle of the

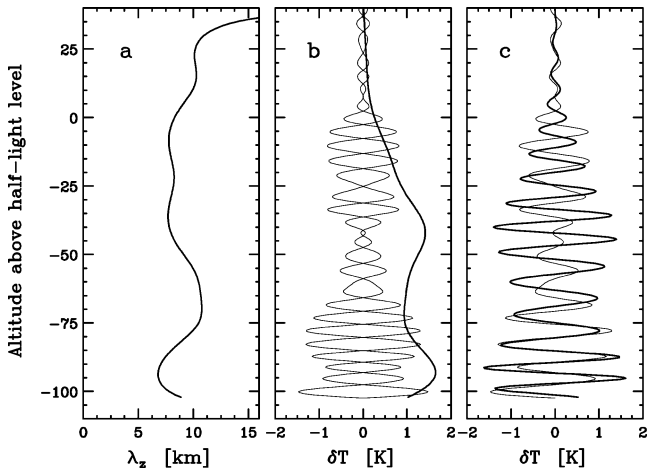


Fig. 13. Same as Fig. 11 but for the 9 km structure.

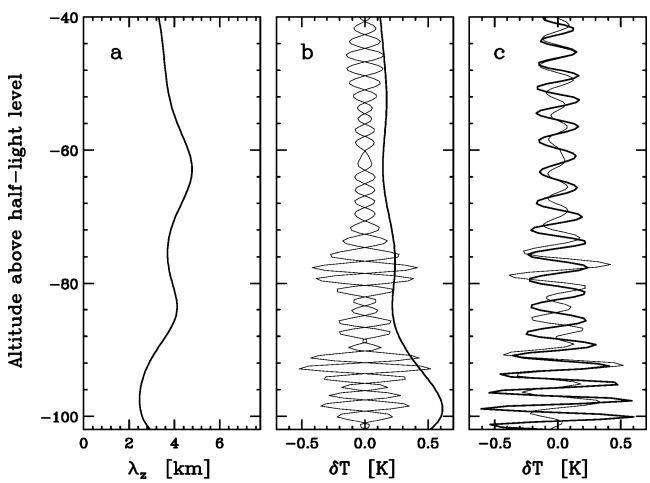


Fig. 14. Same as Fig. 11 but for the 3 km structure.

sampled region, with no significant influence from the edges. The simulation shows (Fig. 11) that the vertical wavelength of a gravity wave that fits the observations at $z = -45$ km varies between $\lambda_{\min} = 12$ km and $\lambda_{\max} = 17$ km throughout the observed region. The reconstructed temperature fluctuations for wavelengths 12 km $< \lambda_z <$ 17 km is compared with the simulation of the wave amplitude. The reconstruction indicates a global maximum at $z = -40$ km with several smaller local maxima at $-90$, $-5$, and 27 km. The presence and the location of a global maximum is indicative for wave dissipation at this altitude. The level of wave dissipation is determined by both vertical and horizontal wavelengths. At this point the horizontal wavelength $\lambda_h$ is undetermined and is treated as a free parameter. In order to be able to fit the reconstructed amplitude, the horizontal wavelength should be $\lambda_h = 750$ km for the chosen eddy diffusion coefficient. The results show an excellent fit to the observed amplitude. Most notably the locations of the secondary maxima and minima are very well predicted by the simulations. These secondary peaks are entirely a result of the non-isothermal structure of the background atmosphere and cannot be artificially adjusted by varying the model parameters. The same amplitude variations are visible in the temperature profile when no dissipation is present in the simulations.

The next step is to compare the phase behavior of the simulated wave and the reconstructed temperature fluctuations (Fig. 11c). Once again we have a rather good agreement between the observations and the simulations with a more notable discrepancy at about $-15$ km below the mid-occultation level where we also over-predict the observed amplitude. This discrepancy could be a result of a small wind shear at this altitude, an effect which we do not include in our simulations.

Based on our analysis of the wave amplitude, vertical scale and phase, we conclude that the temperature fluctuations responsible for the 13.9 km structure in the ingress temperature profile are most likely a result of a propagating atmospheric gravity wave. The maximum wave amplitude is about 1 K. If the actual vertical wavelength is indeed 14 km this wave is not in a saturated regime. The actual vertical wavelength however might differ significantly from the observed one as a result of the slanted phase plane geometry of the wave and the non-radial stellar path through the atmosphere. For more detailed discussion of this ambiguity in the actual wave parameters we refer the reader to Raynaud et al. (2003).

The results from our analysis for the 22, 9, and 3 km peaks are presented in Figs. 12–14, respectively. One can see that we are not able to achieve such a good fit of the observations as for the 14 km structure. The amplitude and the phase of the simulated 22 km wave fit well the observations above $z = -60$ km but fail to explain the data below that level. It is possible that the significant power contained in the large scales below $z = -60$ km reflects stationary features rather than propagating waves.

It is also difficult to reconcile the reconstructed vertical profile of the 9 km structure with a gravity wave model. Although the predicted phase looks in reasonable agreement with the observations the simulated amplitude does not fit the observed temperature fluctuations. It seems unlikely that these fluctuations are caused by an atmospheric gravity wave.

Our simulations of the 3 km structure look more promising. The predicted behavior of the wave phase agrees well with the phase of the reconstructed fluctuations. The simulated wave amplitude profile also captures the overall profile of the observed temperature fluctuations although the agreement is more qualitative than quantitative. Because the observed vertical wavelength of this wave mode is very small there is a concern about the resolution of the observations ($\sim$ 3 km in the upper part of the profiles, $\sim$ 0.5 km at the bottom) and our capability to properly resolve the wave especially at higher altitudes.

It is difficult to apply a similar analysis to the 10.5 km structure in the egress temperature profile. The peak occurs

very close to the bottom of the atmospheric region for which data is available (see Fig. 9), and the wavelet analysis is hindered by strong edge effects.

To summarize the results from the simulations, we believe that the temperature fluctuations with a vertical wavelength of about 14 km are a result of a vertically propagating gravity wave. The temperature amplitude of the wave is about 1 K and is damped by eddy diffusion which significantly exceeds molecular diffusion effects at these altitudes. The wave does not appear to be saturated which is in agreement with the observed vertical wavelength and the small temperature amplitude. The corresponding horizontal wavelength is 750 km and the wave period is 263 min.

The wave reaches a maximum amplitude at a pressure level of 11.5 µbar, about 40 km below the half-light occultation level. By the time the wave reaches this altitude, about 63% of the wave energy is deposited in the background atmosphere as a result of wave dissipation dominated by eddy diffusion. Assuming no significant wind shear, the vertical energy flux of the wave at the level of generation, away from the region of dissipation, is about $0.1\,\mathrm{erg\,cm^{-2}\,s^{-1}}$. Once again, the exact wave parameters and therefore the estimated energy flux carried by the wave cannot be determined uniquely from a single temperature profile. A question also arises about the detectability of periodic atmospheric structures of a relatively short horizontal scale with an occultation technique. As a matter of fact, most of the refraction of the stellar light during an occultation occurs within a finite horizontal region $L = \sqrt{2\pi r H} \approx 3600$ km, where $r$ is the planetary radius. Sicardy et al. (1999) demonstrated that the amplitude of the stellar flux fluctuations resulting from the presence of a monochromatic atmospheric gravity wave with a vertical wavelength $\lambda_z$ and a projection of the horizontal wavelength along the line of sight $l = \lambda_h/\cos\theta_l$, is not significantly reduced if

$$\frac{l}{\lambda_z} > \eta, \quad \eta = \left(\frac{r}{4H}\right)^{0.5}, \tag{2}$$

where $\theta_l$ is the angle of the line of sight with respect to the horizontal direction of wave propagation ($0° < \theta_l < 90°$) and for Jupiter $\eta \approx 25$. Therefore, as long as the above requirement is satisfied, a wave structure is well detectable even if the horizontal wavelength is very small. Equation (2) also suggests that waves propagating at a large angle with respect to the line of sight are easier to detect. In the current study we have no means to determine the horizontal direction of wave propagation and $\theta_l$ is a free parameter. Nevertheless it is easy to see that for a wave with $\lambda_z = 14$ km and $\lambda_h = 750$ km

$$\frac{l}{\lambda_z} \geqslant \frac{\lambda_h}{\lambda_z} = 53 > \eta \tag{3}$$

and (2) is satisfied for any angle of wave propagation.

## 6. Conclusion

A new estimate of the background flux in the 1971 $\beta$ Sco occultation data has allowed us to obtain new temperature profiles for the high southern latitudes ($\sim 60°$) in the jovian atmosphere. The updated value for the pressure scale height ($H = 24 \pm 1.5$ km) brings the observational results of the Meudon group into a better agreement with the observations of the Texas and the Cornell groups. We have demonstrated the usefullness of the continuous wavelet transform for the analysis of small scale structures in the inverted occultation profiles. The temperature gradient profiles, as well as the spectral behavior of the temperature fluctuations, point to the presence of gravity waves in the probed atmospheric region. We have been able to detect several wave modes in the wavelet decomposition of the temperature profiles. The detailed comparison of the observed temperature fluctuations with model-generated gravity waves demonstrates that at least one of the identified wave modes in the ingress profile ($\lambda_z = 13.9$ km) shows a remarquable similarity with the properties of an inertia-gravity wave. French and Gierasch (1974) pointed out the presence of a 13 km wave-like mode in the egress temperature profile that resulted from the lightcurves of the Cornell group (Veverka et al., 1974). There was however no information on the exact vertical profile of the wave amplitude and vertical wavelength. It is possible that the 13 km wave identified by French and Gierasch (1974) corresponds to the 10.5 km wave mode that we detect in our egress wavelet map. A wavelet analysis of the temperature profiles of the Texas and the Cornell groups could allow a comparison between the present wave modes in the different profiles, and in the case of a common wave pattern, the determination of the exact wave parameters.

## Acknowledgments

We thank F. Arenou for his efforts to improve the astrometry of the $\beta$ Sco system, and L. Vapillon for his advice on the 1971 data charts. We are grateful to R. Yelle and an anonymous referee for their help in improving the manuscript. We thank the French Programme National de Planétologie (CNES/INSU) for support in data reduction. KM acknowledges the support by the European Community through the Marie Curie Fellowship Program (contract HPMF-CT-2000-01005). Wavelet software was provided by C. Torrence and G. Compo and is available at URL: http://paos.colorado.edu/research/wavelets/.

## References

Atreya, S.K., 1986. Atmospheres and Ionospheres of the Outer Planets and their Satellites. Springer-Verlag, Heidelberg, New York.

Bartholdi, P., Owen, F., 1972. The occultation of Beta Scorpii by Jupiter and Io. II. Io. Astron. J. 77, 60–64.

Baum, W.A., Code, A.D., 1953. A photometric observation of the occultation of $\sigma$ Arietis by Jupiter. Astron. J. 58 (1208), 108–112.

Berezne, J., Combes, M., Laporte, R., Lecacheux, J., Vapillon, L., 1975. The occultation of $\beta$ Scorpii by Jupiter III. Discussion of the photometric results. Astron. Astrophys. 40, 85–90.

Combes, M., Lecacheux, J., Vapillon, L., 1971. First results of the occultation of $\beta$ Sco by Jupiter. Astron. Astrophys. 15, 235–238.

Drossart, P., Sicardy, B., Roques, F., Widemann, T., Gladstone, R., Waite, J.H., Vincent, M., 2000. The methane homopause of Jupiter seen from the IR spectroscopy of star HIP 9369 during its occultation by Jupiter. Bull. Am. Astron. Soc. 32, 1013.

Farge, M., 1992. Wavelet transforms and their application to turbulence. Annu. Rev. Fluid Mech. 24, 395–457.

French, R.G., Gierasch, P.J., 1974. Waves in the jovian upper atmosphere. J. Atmos. Sci. 31, 1707–1712.

French, R.G., Elliot, J.L., Gierasch, P.J., 1978. Analysis of stellar occultation data: effects of photon noise and initial conditions. Icarus 33, 186–202.

Hanel, R., Conrath, B., Flasar, M., Herath, L., Kunde, V., Lowman, P., Maguire, W., Pearl, J., Pirraglia, J., Horn, H., 1979. Infrared observations of the jovian system from Voyager 2. Science 206, 952–956.

Hinson, D.P., Jenkins, J.M., 1995. Magellan radio occultation measurements of atmospheric waves on Venus. Icarus 114, 310–327.

Hubbard, W.B., Van Flandern, T.C., 1972. The occultation of $\beta$ Scorpii by Jupiter and Io III. Astrometry. Astron. J. 77, 65–74.

Hubbard, W.B., Nather, R.E., Evans, D.S., Tull, R.G., Wells, D.C., van Citters, G.W., Warner, B., Vanden Bout, P., 1972. The occultation of Beta Scorpii by Jupiter and Io. I. Jupiter. Astron. J. 77 (1), 41–59.

Hubbard, W.B., Haemmerle, V., Porco, C.C., Rieke, G.H., Rieke, M.J., 1995. The occultation of SAO 78505 by Jupiter. Icarus 113, 103–109.

Lecacheux, J., Combes, M., Vapillon, L., 1973. The $\beta$ Scorpii occultation by Jupiter I. The jovian diameter. Astron. Astrophys. 22, 289–292.

Lindzen, R.S., 1981. Turbulence and stress owing to gravity wave and tidal breakdown. J. Geophys. Res. 86, 9707–9714.

Matcheva, K.I., Strobel, D.F., 1999. Heating of Jupiter's thermosphere by dissipation of gravity waves due to molecular viscosity and heat conduction. Icarus 140, 328–340.

Matcheva, K.I., Strobel, D.F., Flasar, F.M., 2001. Interaction of gravity waves with ionospheric plasma: implications for Jupiter's ionosphere. Icarus 152, 347–365.

Orton, G.S., Friedson, A.J., Caldwell, J., Hammel, H.B., Baines, K.H., Bergstrahl, J.T., Martin, T.Z., Malcolm, M.E., West, R.A., Golish, W.F., Griep, D.M., Kaminsky, C.D., Tokunaga, A.T., Baron, R., Shure, M., 1991. Thermal maps of Jupiter: spatial organisation and time dependence of stratospheric temperatures, 1980–1990. Science 252, 537–542.

Raynaud, E., Drossart, P., Matcheva, K., Sicardy, B., Hubbard, W.B., Roques, F., Widemann, Th., Gladstone, G.R., Waite, J.H., Nadeau, D., Bastien, P., Doyon, R., Hill, R., Rieke, M.J., Marley, M., 2003. The 10 October 1999 HIP 9369 occultation by the northern polar region of Jupiter: ingress and egress lightcurves analysis. Icarus 162, 344–361.

Roques, F., Sicardy, B., French, R.G., Hubbard, W.B., Barucci, A., Bouchet, P., Brahic, A., Gehrels, J.A., Gehrels, T., Grenier, I., Lebertre, T., Lecacheux, J., Maillard, J.P., McLaren, R.A., Perrier, C., Vilas, F., Waterworth, M.D., 1994. Neptune's upper stratosphere, 1983–1990: ground-based stellar occultation observations III. Temperature profiles. Astron. Astrophys. 288, 985–1011.

Seiff, A., Kirk, D.B., Knight, T.C.D., Mihalov, J.D., Blanchard, R.C., Young, R.E., Schubert, G., von Zahn, U., Lehmacher, G., Milos, F.S., Wang, J., 1996. Structure of the atmosphere of Jupiter: Galileo probe measurements. Science 272, 844–845.

Sicardy, B., Ferri, F., Roques, F., Lecacheux, J., Pau, S., Brosch, N., Nevo, Y., Hubbard, W.B., Reitsema, H.J., Blanco, C., Carreira, E., Beisker, W., Bittner, C., Bode, H.-J., Bruns, M., Denzau, H., Nezel, M., Riedel, E., Struckman, H., Appleby, G., Forrest, R.W., Nicolson, I.K.M., Hollis, A.J., Miles, R., 1999. The structure of Titan's stratosphere from the 28 Sgr occultation. Icarus 142, 357–390.

Smith, S.A., Fritts, D.C., VanZandt, T.E., 1987. Evidence for a saturated spectrum of atmospheric gravity waves. J. Atmos. Sci. 44 (10), 1404–1410.

Torrence, C., Compo, G.P., 1998. A practical guide to wavelet analysis. Bull. Am. Meteor. Soc. 79, 61–78.

Vapillon, L., Combes, M., Lecacheux, J., 1973. The $\beta$ Scorpii occultation by Jupiter. II. The temperature and density profiles of the jovian upper atmosphere. Astron. Astrophys. 29, 135–149.

Veverka, J., Wasserman, L.H., Elliot, J., Sagan, C., 1974. The occultation of $\beta$ Scorpii by Jupiter I. The structure of the jovian upper atmosphere. Astron. J. 79, 73–84.

Wasserman, L., Veverka, J., 1973. On the reduction of occultation light curves. Icarus 20, 322–345.

Yelle, R.V., Griffith, C.A., Young, L.A., 2001. Structure of the jovian stratosphere at the Galileo probe entry site. Icarus 152, 331–346.

Young, L.A., Yelle, R.V., Young, R., Seiff, A., Kirk, D.B., 1997. Gravity waves in Jupiter's thermosphere. Science 276, 108–110.

Young, L.A., Bosh, A.S., Buie, M., Elliot, J.L., Wasserman, L.H., 2001. Uranus after solstice: results from the 1998 November 6 occultation. Icarus 153, 236–247.

von Zahn, U., Hunten, D.M., Lehmacher, G., 1998. Helium in Jupiter's atmosphere: results from the Galileo probe Helium Interferometer Experiment. J. Geophys. Res. 103, 22815–22829.